2   "Integrated geophysical characterization of crustal domains in the Eastern

3   Black Sea"

4   **Vanessa Monteleone[1, 2], Tim A. Minshull[1], and Hector Marin-Moreno[2]**

5   *[1] School of Ocean and Earth Science, University of Southampton, National Oceanography*

6   *Centre Southampton, Waterfront Campus, European Way, Southampton SO14 3ZH, UK*

7   *(v.monteleone@soton.ac.uk; tmin@noc.soton.ac.uk).*

8   *[2]National Oceanography Centre, University of Southampton Waterfront Campus, European*

9   *Way, Southampton SO14 3ZH, UK (hector.marin.moreno@noc.ac.uk).*

10

11   **Content of this file**

12   Text: Details of Methods

13   -   Seismic Data

14   -   Magnetic Anomaly Data

15   -   Magnetic Anomaly Modelling

16   -   Magnetic Anomaly Filtering

17   -   Method Limitations and Data Dependency

18   Text: References

19   Table DR1

20   Figures DR1 to DR8

21   **DETAILS OF METHODS**

22   **Seismic Data**

23   Twelve post-stack time-migrated seismic reflection profiles are used in this study (Fig. DR1,

24   DR2). The dataset was acquired in 2011 by Geology Without Limits (GWL) and ION GXT.

25   Table DR1 provides information about the acquisition parameters and the processing steps

26   carried out by GWL.

2011 Long-Offset - Acquisition parameters					
Source		Streamer		Recorder	
Array volume	5680 cu.in	Length	10200 m	Sampling rate	2.0 ms
shot interval	50 m	Channels	860	Record length	18 sec
Depth	8 m ± 0.5 m	Receiver spacing	12.5 m	Filters LC	3 Hz
Pressure	2000 PSI	Depth	9 m ± 0.5 m	Filters HC	200 Hz
		Offset min	149.5 m		
		Offset max	10500 m		

27

28

Processing steps
segy input and geometry application
Spherical divergence correction
Velocity analysis
Predictive deconvolution 8 ms, 240 ms, wn 1%
Radon demultiple
Amplitude balancing
NMO muting and stacking
Kirchhoff migration
BP filter 4-8-100-120 Hz
Coherent filtering
Amplitude balancing

29

30

31

32

33

34

35

36   **Table DR1.** Top) Summary of the 2D long-offset seismic reflection profiles acquisition

37   parameters; bottom) GWL processing steps used to generate the post-stack time migrated

38   profiles.

39

40   We converted time migrated profiles into depth using interval velocities derived from GWL

41   stacking velocities, combined with wide-angle tomographic velocities from Shillington et al.

42   (2009). A comparison between the two velocity trends shows that velocities above basement

43   reflection are similar, but stacking velocities are widespread across the study region and they

44   better follow geological variations across seismic sections. Below basement, stacking velocities

45   have a single, low-velocity, and linearly increasing trend, whereas wide-angle data show faster

46   velocity trends with more realistic gradient changes, making them more reliable at depths below

47   basement.

48   Velocity model creation was performed on Petrel 2015 software. Seismically interpreted

49   horizons, corresponding to main acoustic impedance contrasts, were used to define a four-layer

50   model. Each layer was defined by a V0 velocity (top layer velocity) representing the averaged

51   stacking/wide-angle velocities along the layer-bounding horizons. A mean velocity gradient was

52   estimated between top and bottom layer velocities and applied to the model. Further information

53   about the velocity model creation, and time-depth conversion steps is given by Monteleone et al.

54   (2019).

55

56   **Magnetic Anomaly Data**

57   We used the Earth Magnetic Anomaly Grid (EMAG2-v3, www.NOAA.gov) over the EBSB

58   region (Fig. DR2), which is specified as a 2-arc-minute resolution grid of the total intensity

59   magnetic anomaly at an altitude of 4 km above mean sea level, and it is compiled from satellite,

60   marine, aero-magnetic and ground magnetic surveys (Maus et al., 2009; Meyer et al., 2017).

61   A reduction-to-pole (RTP) transform was applied to the magnetic anomaly grid. RTP reduces the

62   magnetic anomalies to the pole and corrects for variations in inclination and declination over the

63   study area (Baranov, 1957). Declination, inclination, and magnitude of the modern Earth's

64   magnetic field were taken according to IGRF field (Thébault et al., 2015). RTP was applied to

65   the total intensity magnetic map using a declination of 6° and an inclination of 61° at the center

66   of the EBSB.

67

68   **Magnetic Anomaly Modelling**

69   Inverse modeling of magnetic anomalies is generally used when well-defined constraints are

70   available (e.g., Parker and Huestis, 1974; Russell and Whitmarsh, 2003). Such inverse models

71   result in calculated anomalies that match closely those observed, including those resulting from

72   3D effects, and inverse models of 2D profiles will not normally match at profile crossings. To

73   avoid over-fitting the data, and to ensure that models of crossing profiles are consistent with each

74   other, we use a forward modeling approach. Due to the inherent non-uniqueness of such forward

75   models, we kept them simple and made no attempt to produce perfect fits of the observed

76   anomalies. Such a forward modeling approach has been used commonly along continental

77   margins elsewhere (e.g., Bronner et al., 2011; Rippington et al., 2015).

78   Forward modelling was undertaken using Geosoft software, Oasis Montaj V9.4 along the seismic

79   profiles. These models were built from SEG-Y files of the seismic data and modelled against the

80   gridded potential field data sampled along the corresponding sections. Our 2D models assume

81   that there are no variations perpendicular to the profiles. However, because the observed

82   anomaly results from 3D effects, we include the anomaly variations within about 15 km either

83   side of the magnetic profiles (grey bands; Fig. DR2-7). The choice of a 15 km range is due to the

84   high geological variability perpendicular to the magnetic profiles. Ranges > 15 km would

4

85   introduce anomaly trends from different crustal structures domains, especially along the NW-SE-

86   trending profiles.

87   Magnetic anomaly profiles were extracted from the RTP EMAG2-v3 grid, and used to

88   complement seismic sections (Fig. DR2-7). Modelling was constrained by the top basement

89   reflection interpreted from seismic data. Because the sedimentary cover has a very low

90   magnetization in the Black Sea region (e.g., Ross, 1978), modelling was done considering the

91   upper boundary of the magnetized layer to coincide with the top basement. Crustal layers and

92   magmatic bodies modelled along the top basement were assumed to have attained their

93   magnetization during the Late Cretaceous and/or Early Cenozoic (e.g., Nikishin et al., 2015) at

94   approximately their present latitude, so no paleo-latitude correction was applied in this study. No

95   susceptibility data are available for the central EBSB, and little information is available from

96   values of magnetic susceptibility of adjacent onshore samples (e.g., Rangin et al., 2002;

97   Hippolyte et al., 2010). Thus, we were guided by average values of magnetization estimated for

98   different type of magnetized rocks (e.g., Hunt et al., 1995).

99   We started with the simplest possible model characterized by a non-magnetized sedimentary

100   layer and a uniformly and weakly-magnetized crustal layer (0.05 A/m). For crustal thickness (top

101   basement to Moho depth), we used results from both wide-angle data (Shillington et al., 2009)

102   and gravity modelling (Graham et al., 2013). Studies of the Curie temperature (578° C -

103   temperature above which magnetite loses its magnetic properties) in the Black Sea region show

104   that the Curie depth is reached mainly below Moho but sometimes above it, in a depth range of

105   24-36 km (e.g., Starostenko et al., 2014; Aydin et al., 2005; Maden, 2013). Since we are mostly

106   concerned with regions where the Moho is shallower than 24 km, we assumed in this initial

107   model that all the EBSB crust is magnetized.

108   A crustal magnetization of 0.05 A/m had a limited contribution to the calculated anomaly and the

109   observed anomaly was mostly determined by higher magnetizations near the top of basement.

110   Magnetic modeling is usually performed either assuming a fixed value of magnetization and a

111   variable thickness for the magnetized layer, or a fixed layer thickness and variable magnetization

112   intensities along it (e.g., Banerjee, 1984). In the EBSB, there are no available independent

113   constraints on the thickness or the intensity of magnetic sources. Our strategy was to find a

114   simple model that could be mechanistically justified and was able to simulate the observed

115   magnetic anomaly (Fig. DR2-7). We limited the magnetizations to values representative of felsic

116   to mafic igneous rocks (0.2-5.0 A/m; e.g., Hunt et al., 1995) and assumed a constant-thickness

117   magnetized layer subdivided into bands/blocks of variable magnetization, with its top coinciding

118   with the seismically-inferred basement. This type of approach is common, particularly at rifted

119   continental margins (e.g., Banerjee, 1984; Bronner et al., 2011; Collier et al., 2017). In oceanic

120   domains, magnetic layer thicknesses of 0.5 km (e.g., Hussenoeder et al., 1996; Searle et al.,

121   2010), 1.0 km (e.g., Ozima et al., 1974; Searle et al., 1998), 1.5 km (e.g., Bronner et al., 2011), or

122   2.0 km (e.g., Collier et al., 2017) are generally used. Changes in magnetized layer thickness will

123   affect the intensity of the magnetization inferred (almost inversely proportional to thickness), but

124   will change little the overall trend of the modeled anomaly (e.g., Parker and Huestis, 1974). In

125   this study, we exclude thin magnetized layers of a few hundred meters that would require

126   anomalously high magnetizations to model the observed anomaly. We use a 1 km-thick layer in

127   the oceanic domain because it is consistent with similar work elsewhere and allows us to

128   generate a model with reasonable magnetizations.

129   Since no independent constraints are available on the thickness of the magnetized layer over the

130   structural highs (Shatsky Ridge and MBSH), and because these areas are only modeled to

131 provide lateral constraints for the central basin magnetic model, we decided to keep the same

132 constant layer thickness in order to generate a simple and consistent model along the profiles.

133 Volcanic bodies imaged in seismic reflection data (e.g., Nikishin et al., 2003, 2015), and high-

134 density bodies interpreted from gravity modelling (e.g., Starostenko et al., 2004), helped to

135 constrain the distribution of these magnetized bodies and those along the basin margins during

136 the main rifting phase. Based on these assumptions, we updated the starting model to fit

137 adequately the observed field.

138

139 **Magnetic Anomaly Filtering**

140 A low-pass filter was applied to the calculated anomaly to remove wavelengths shorter than a

141 specified cut-off, thus removing the result of a short-wavelength crustal anomalies such as those

142 caused by local variations of the top basement horizon picked along seismic profiles. We chose a

143 low-pass wavelength cut-off of 25 km. This cut-off allows us to remove some short-period

144 oscillations from the calculated anomaly without removing lateral variations that fall within the

145 wavelength of the observed anomaly. A cut-off > 25 km was observed to remove information

146 resolved by the magnetic anomaly grid (Fig. DR8).

147

148 **Method Limitations and Data Dependency**

149 The non-uniqueness of the potential field problem requires introducing assumptions such as

150 simplification of geometry, limits to size or depth, and range limits on

151 susceptibility/magnetization values (Paterson and Reeves, 1985). Interpretation of magnetic

152 anomaly may be ambiguous, as any given anomaly could be caused by several possible sources.

153 For example, the amplitude and shape of an anomaly produced by a large body at great depth can

154   be similar to that of a small body closer to the surface. Changes in depth, shape, and position of

155   the top basement horizon picked from seismic profiles and used as top boundary for the model

156   creation can also affect the resulting calculated anomaly. In addition, attempting to model

157   gridded magnetic data in 2D neglects the fact that the observed data could be affected by features

158   that are out of the plane of the modeled section (3D effects) that make fitting these data very

159   difficult at some locations (e.g., Rippington et al., 2015).

160   Despite all its limitations, 2D forward magnetic anomaly modeling can provide a quantitative

161   perspective to features visible on seismic data and aid the interpretation in areas where seismic

162   imaging is difficult. The non-uniqueness of the magnetic problem can be reduced in several

163   ways. For example, having an even distribution of seismic lines across the area helps ensuring

164   that any interpretation made on either the seismic or magnetic datasets can be calibrated to and

165   constrained by the other. By interpreting features that fit both independent datasets we can

166   increase the confidence in that interpretation. Also, geological knowledge and literature

167   information is required to produce a reasonable set of modelling parameters.

168   Here magnetic anomaly modelling allows us to estimate regional scale variations in the

169   magnetization character of crustal elements without specifically correlating small wavelength

170   anomalies to a precise causative body. Although any conclusion inferred from magnetic

171   modelling is strongly model dependent, because of the ambiguity in crustal affinity at the center

172   of the EBSB shown by seismic reflection and refraction data, our magnetic modelling results

173   provide additional and effective insights into crustal affinity and distribution in the center of the

174   EBSB.

175   **REFERENCES**

176   Aydın, İ., Karat, H. İ., and Koçak, A., 2005, Curie-point depth map of Turkey. Geophysical

177   Journal International, 162(2), 633-640. https://doi.org/10.1111/j.1365-246X.2005.02617.x

178   Banerjee, S. K., 1984, The magnetic layer of the ocean crust—How thick is it?. Tectonophysics,

179   105(1-4), 15-27. https://doi.org/10.1016/0040-1951(84)90191-4

180   Baranov, V., 1957, A new method for interpretation of aeromagnetic maps: pseudo-gravimetric

181   anomalies. Geophysics, 22(2), 359-382. https://doi.org/10.1190/1.1438369

182   Bronner, A., Sauter, D., Manatschal, G., Péron-Pinvidic, G., and Munschy, M., 2011, Magmatic

183   breakup as an explanation for magnetic anomalies at magma-poor rifted margins. Nature

184   Geoscience, 4(8), 549. DOI: 10.1038/NGEO1201

185   Collier, J. S., McDermott, C., Warner, G., Gyori, N., Schnabel, M., McDermott, K., and Horn, B.

186   W., 2017, New constraints on the age and style of continental breakup in the South Atlantic

187   from magnetic anomaly data. Earth and Planetary Science Letters, 477, 27-40.

188   https://doi.org/10.1016/j.epsl.2017.08.007

189   Graham, R., Kaymakci, N., and Horn, B. W., 2013, The Black Sea: something different. Geo

190   Expro, 10(5), 57-62.

191   Hippolyte, J. C., Müller, C., Kaymakci, N., and Sangu, E., 2010, Dating of the Black Sea Basin:

192   new nannoplankton ages from its inverted margin in the Central Pontides (Turkey).

193   Geological Society, London, Special Publications, 340(1), 113-136.

194   https://doi.org/10.1144/SP340.7

195   Hunt, C. P., Moskowitz, B. M., and Banerjee, S. K., 1995, Magnetic properties of rocks and

196   minerals. Rock physics & phase relations: a handbook of physical constants, 3, 189-204.

197   https://doi.org/10.1029/RF003p0189

198   Hussenoeder, S. A., Tivey, M. A., Schouten, H., and Searle, R. C., 1996, Near- bottom magnetic

199   survey of the Mid- Atlantic Ridge axis, 24°–24° 40′ N: Implications for crustal accretion at

200   slow spreading ridges. Journal of Geophysical Research: Solid Earth, 101(B10), 22051-

201   22069. https://doi.org/10.1029/96JB01890

202   Maden, N., 2013, Geothermal structure of the eastern Black Sea basin and the eastern Pontides

203   orogenic belt: Implications for subduction polarity of Tethys oceanic lithosphere.

204   Geoscience Frontiers, 4(4), 389-398. https://doi.org/10.1016/j.gsf.2013.02.001

205   Maus, S., et al., 2009, EMAG2: A 2–arc min resolution Earth Magnetic Anomaly Grid compiled

206   from satellite, airborne, and marine magnetic measurements. Geochemistry, Geophysics,

207   Geosystems, 10(8). doi:10.1029/2009GC002471

208   Meyer, B., Saltus, R., and Chulliat, A., 2017, EMAG2: Earth Magnetic Anomaly Grid (2-arc-

209   minute resolution) Version 3. National Centers for Environmental Information, NOAA.

210   Model. doi:10.7289/V5H70CVX

211   Monteleone, V., Minshull, T. A., and Marin-Moreno, H., 2019, Spatial and temporal evolution of

212   rifting and continental breakup in the Eastern Black Sea Basin revealed by long-offset

213   seismic reflection data, Tectonics, 38, 2646-2667. doi: 10.1029/2019TC005523.

214   Nikishin, A. M., Korotaev, M. V., Ershov, A. V., and Brunet, M. F., 2003, The Black Sea basin:

215   tectonic history and Neogene–Quaternary rapid subsidence modelling. Sedimentary

216   Geology, 156(1-4), 149-168. https://doi.org/10.1016/S0037-0738(02)00286-5

217   Nikishin, A. M., Okay, A. I., Tüysüz, O., Demirer, A., Amelin, N., and Petrov, E., 2015, The

218   Black Sea basins structure and history: New model based on new deep penetration regional

219   seismic data. Part 1: Basins structure and fill. Marine and Petroleum Geology, 59, 638-655.

220   https://doi.org/10.1016/j.marpetgeo.2014.08.017

221   Ozima, M., Joshima, M., and Kinosmta, H., 1974, Magnetic properties of submarine basalts and

222   the implications on the structure of the oceanic crust. Journal of geomagnetism and

223   geoelectricity, 26(3), 335-354. https://doi.org/10.5636/jgg.26.335

224   Parker, R. L., and Huestis, S. P., 1974, The inversion of magnetic anomalies in the presence of

225   topography. Journal of Geophysical Research, 79(11), 1587-1593.

226   https://doi.org/10.1029/JB079i011p01587

227   Paterson, N. R., and Reeves, C. V., 1985, Applications of gravity and magnetic surveys: The

228   state-of-the-art in 1985. Geophysics, 50(12), 2558-2594. https://doi.org/10.1190/1.1441884

229   Rippington, S., Mazur, S., and Warner, J., 2015, The crustal architecture of the Faroe–Shetland

230   Basin: insights from a newly merged gravity and magnetic dataset. Geological Society,

231   London, Special Publications, 421(1), 169-196. https://doi.org/10.1144/SP421.10

232   Russell, S. M., and Whitmarsh, R. B., 2003, Magmatism at the west Iberia non-volcanic rifted

233   continental margin: evidence from analyses of magnetic anomalies. Geophysical Journal

234   International, 154(3), 706-730. https://doi.org/10.1046/j.1365-246X.2003.01999.x

235   Rangin, C., Bader, A. G., Pascal, G., Ecevitoğlu, B., and Görür, N., 2002, Deep structure of the

236   Mid Black Sea High (offshore Turkey) imaged by multi-channel seismic survey

237   (BLACKSIS cruise) 1, 2. Marine Geology, 182(3-4), 265-278.

238   https://doi.org/10.1016/S0025-3227(01)00236-5

239   Ross, D. A., 1978, Summary of results of Black Sea drilling. Initial Reports of the Deep Sea

240   Drilling Project, 42(Part 2).

241   Searle, R. C., Cowie, P. A., Mitchell, N. C., Allerton, S., MacLeod, C. J., Escartin, J., Russell, S.

242   M., Slootweg, P. A. and Tanaka, T., 1998, Fault structure and detailed evolution of a slow

243   spreading ridge segment: The Mid-Atlantic Ridge at 29 N. Earth and Planetary Science

244   Letters, 154(1-4), 167-183. https://doi.org/10.1016/S0012-821X(97)00160-X

245   Searle, R. C., Murton, B. J., Achenbach, K., LeBas, T., Tivey, M., Yeo, I., et al., 2010, Structure

246   and development of an axial volcanic ridge: Mid-Atlantic Ridge, 45 N. Earth and Planetary

247   Science Letters, 299(1-2), 228-241. https://doi.org/10.1016/j.epsl.2010.09.003

248   Shillington, D. J., Scott, C. L., Minshull, T. A., Edwards, R. A., Brown, P. J., and White, N.,

249   2009, Abrupt transition from magma-starved to magma-rich rifting in the eastern Black Sea.

250   Geology, 37(1), 7-10. doi: 10.1130/G25302A

251   Starostenko, V. I., Dolmaz, M. N., Kutas, R. I., Rusakov, O. M., Oksum, E., Hisarli, Z. M.,

252   Okyar, M., Kalyoncuoglu, U. Y., Tunursatar, H. E. and Legostaeva, O. V., 2014, Thermal

253   structure of the crust in the Black Sea: comparative analysis of magnetic and heat flow data.

254   Marine Geophysical Research, 35(4), 345-359. doi: 10.1007/s11001-014-9224-x

255   Starostenko, V., Buryanov, V., Makarenko, I., Rusakov, O., Stephenson, R., Nikishin, A.,

256   Georgiev, M., Dimitriu, R., Legostaeva, O., Pchelarov, V. and Sava, C., 2004, Topography

257   of the crust–mantle boundary beneath the Black Sea Basin. Tectonophysics, 381(1-4), 211-

258   233. https://doi.org/10.1016/j.tecto.2002.08.001

259   Thébault, E., et al., 2015, International geomagnetic reference field: the 12th generation. Earth,

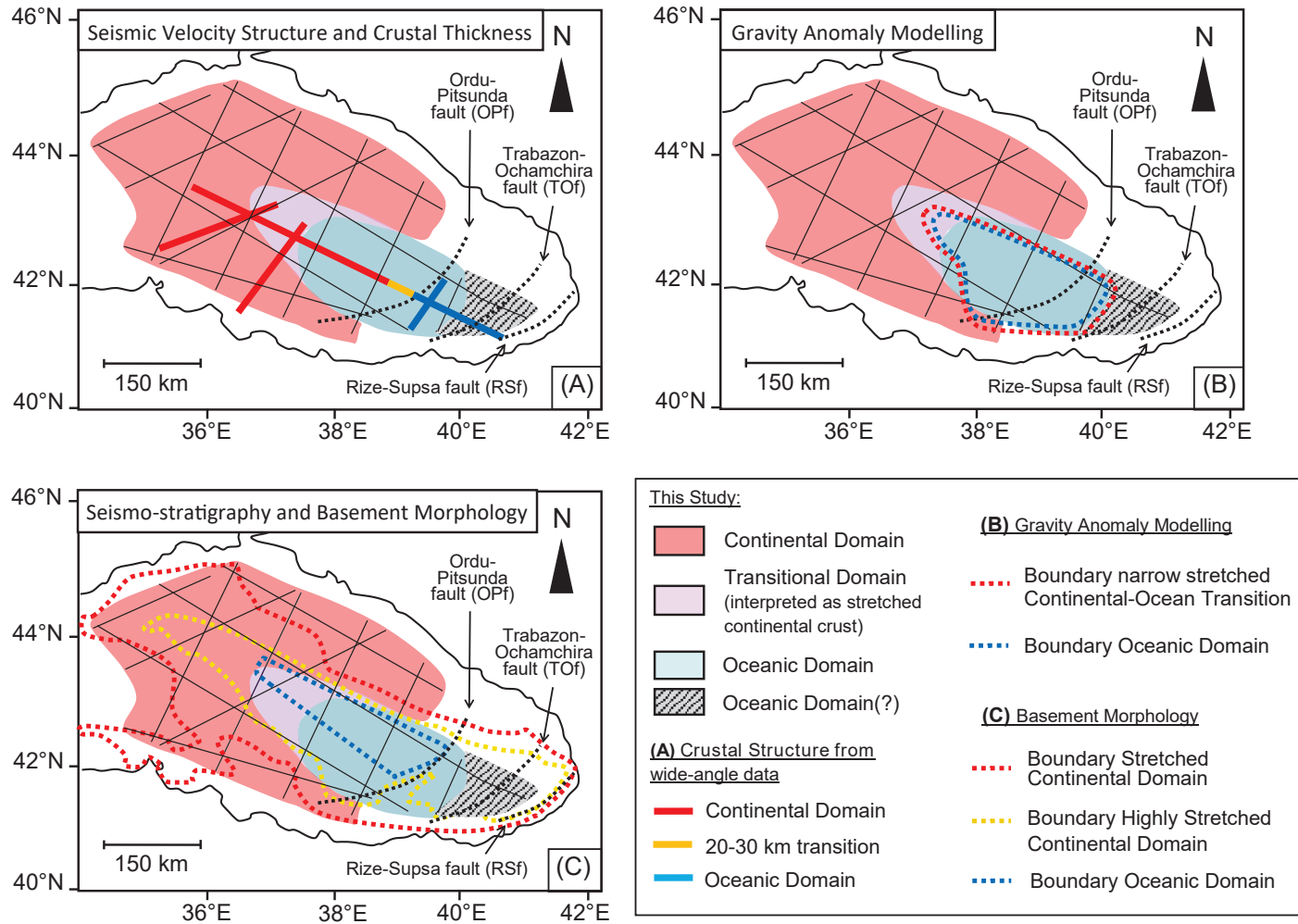260   Planets and Space, 67(1), 79. DOI 10.1186/s40623-015-0228-9

Figure DR1. Comparison between crustal domains boundaries inferred in this study and crustal distribution from other studies using: (A) crustal thickness and lower crustal velocities from wide-angle seismic data (Shillington et al., 2009); (B) gravity anomaly modelling constrained by 2D long-offset seismic reflection profiles (Graham et al., 2013); (C) 2D long-offset seismic reflection profiles interpretation (Nikishin et al., 2015). Note that the extent of oceanic and transitional domains, and the nature of the transition, varies from study to study. In (A), an abrupt, 20-30 km transition from stretched continental to thick oceanic crust is attributed to an along-axis change from magma-poor to magma-rich margin (Shillington et al., 2009); in (B), an extremely abrupt transition zone surrounds the interpreted oceanic domain, and is associated to a ribbon of continental crust intruded by magmatic rocks (Graham et al., 2013); in (C), a wide area of highly-stretched continental crust constitutes the transition to a narrow and elongated, NW-SE-trending oceanic domain (Nikishin et al., 2015). Background colors and colors used to plot crustal distribution/boundaries are explained in the legend.

13
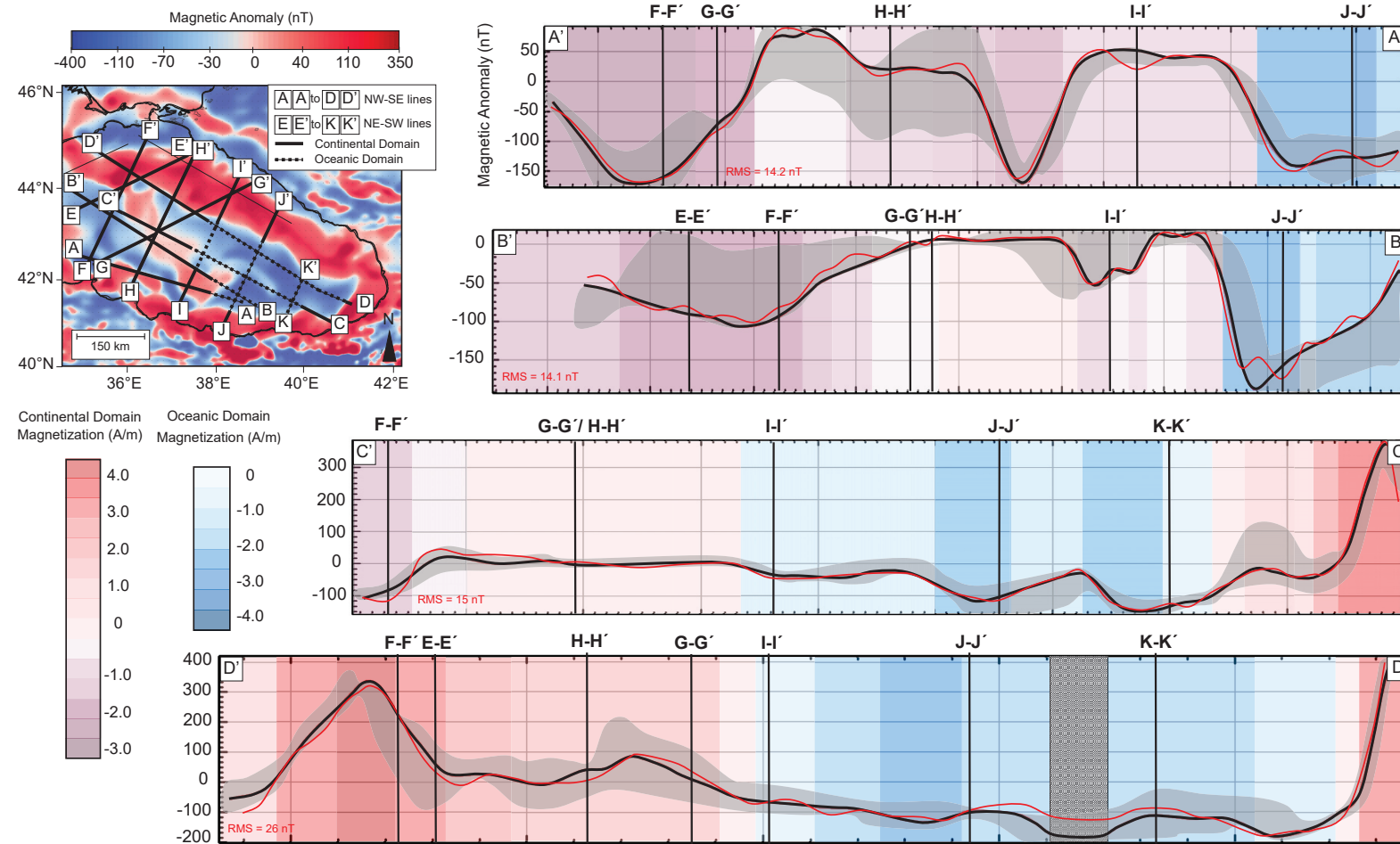
Figure DR2. Magnetic anomaly models along each relevant seismic profile. On the top left corner, the magnetic anomaly map for the EBSB region (RTP EMAG2-v3), with seismic profiles in overlay: thick black lines are modelled profiles where continental crust has been interpreted; thick dotted lines are modelled profiles where oceanic crust has been interpreted. Profiles from A to D are NW-SE trending lines, whereas profiles from E to K are NE-SW trending lines. Each panel compares the calculated (red line) and observed (black line) anomalies. The grey band along the observed anomaly represents the anomaly variations about 15 km either side of the profile. The root mean-squared (RMS) error, expressed in nT, between observed and calculated anomaly is shown at the bottom left corner of each panel. Colored backgrounds along displayed profiles show magnetization intensities for the positively magnetized continental layers (pink), negatively magnetized continental layers (purple), and negatively magnetized oceanic layers (blue). Black vertical lines within each panel show profile intersections. The striped shading over the D-D' profile indicates a gap along the bs-180 seismic line.
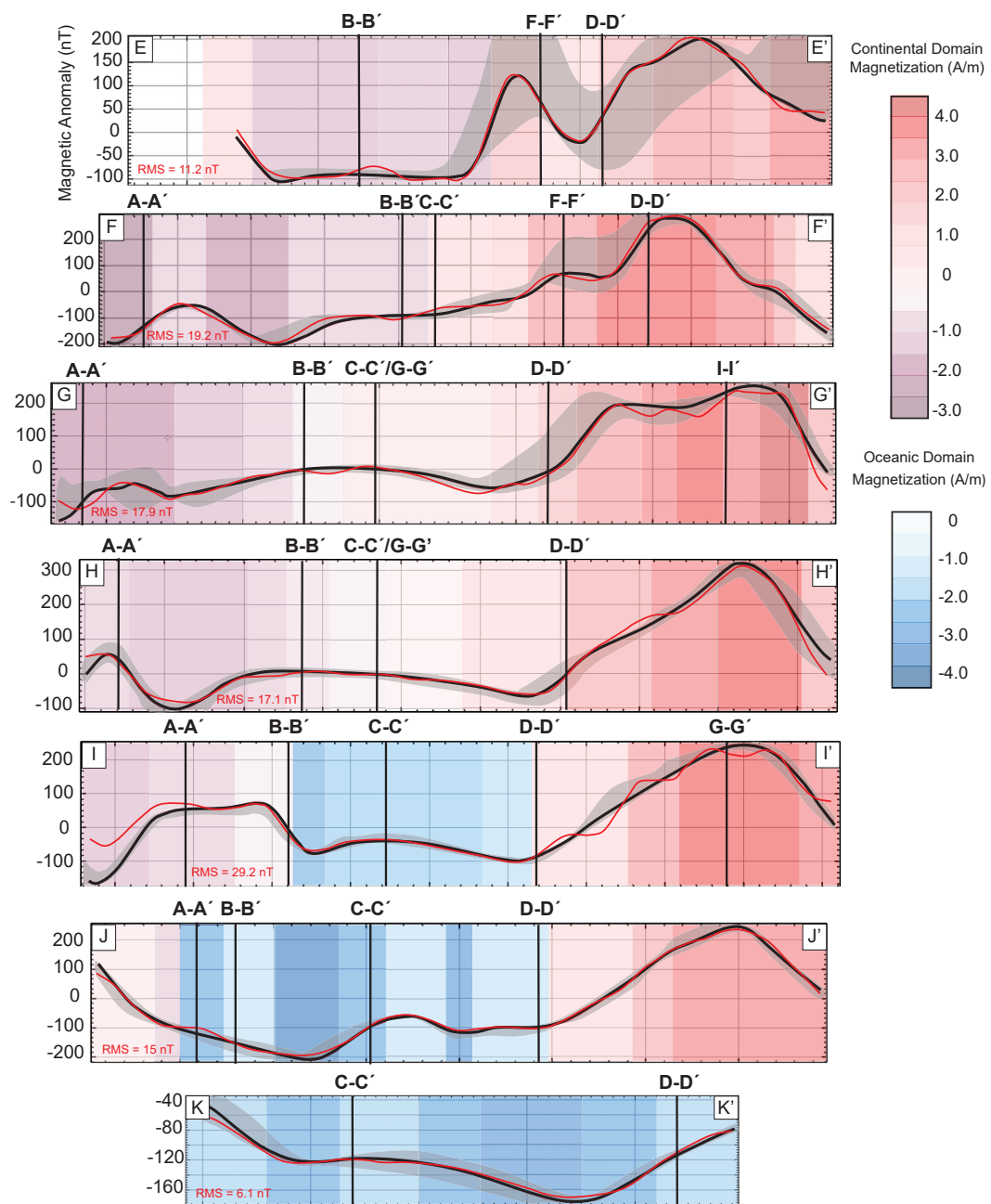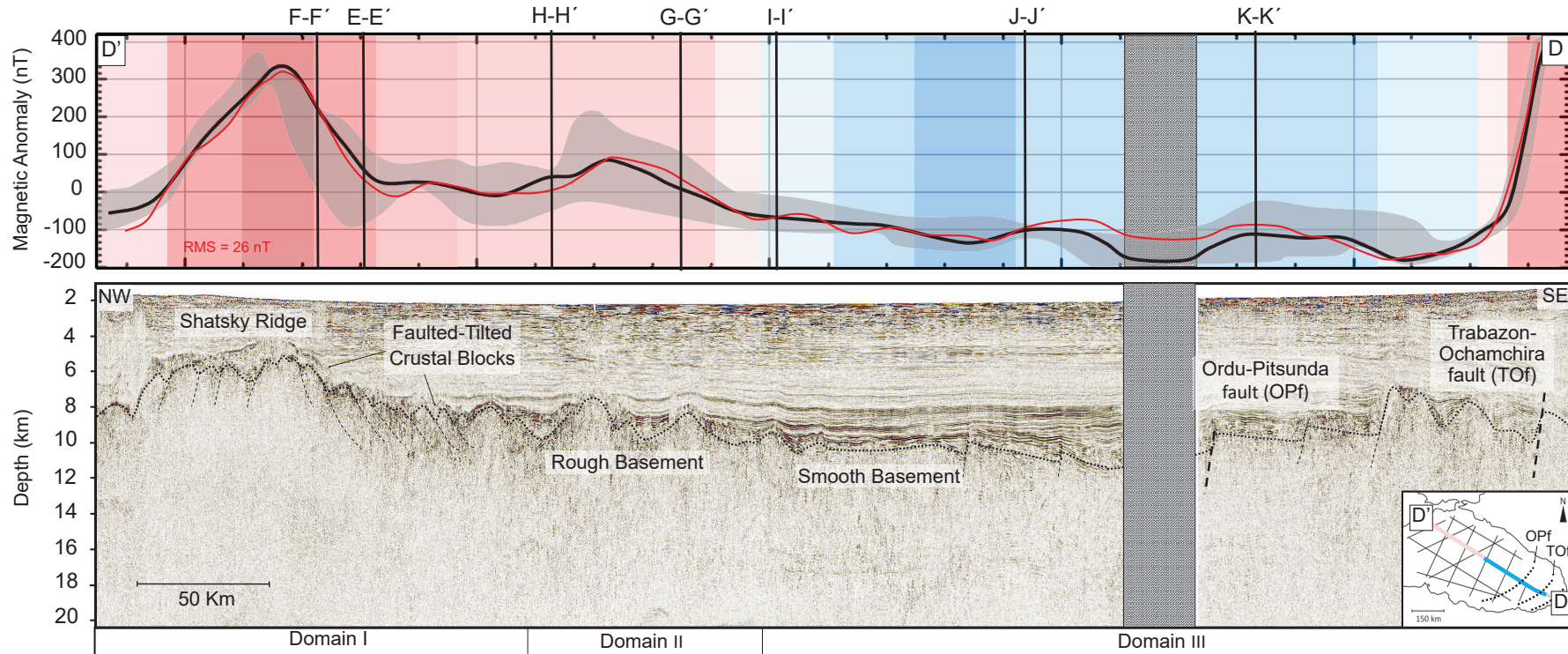
14

Figure DR2. Continued..

Figure DR3. Magnetic anomaly modelling along seismic profile bs-180. Top panel (Fig. DR2 - D-D') shows the observed (black) and calculated (red) anomaly along this profile. Magnetic intensity is indicated with colored bands (color scale as shown in Fig. DR2). Bottom panel shows the bs-180 seismic profile. Top basement and fault systems interpreted are in overlay. This profile shows the transition from the tilted and faulted blocks of the stretched continental domain (Domain I), to the rough, non-faulted continental basement (Domain II), to the smooth oceanic basement affected by trans-tensional faults (Domain III). The striped shading over the two panels indicates a gap along the seismic profile. The location map at the bottom right corner shows the profile position, with colors associated to the interpreted continental (pink) and oceanic (blue) domains. Trans-tensional faults locations are also shown in the location map (OPf and TOf). (VE = 7)
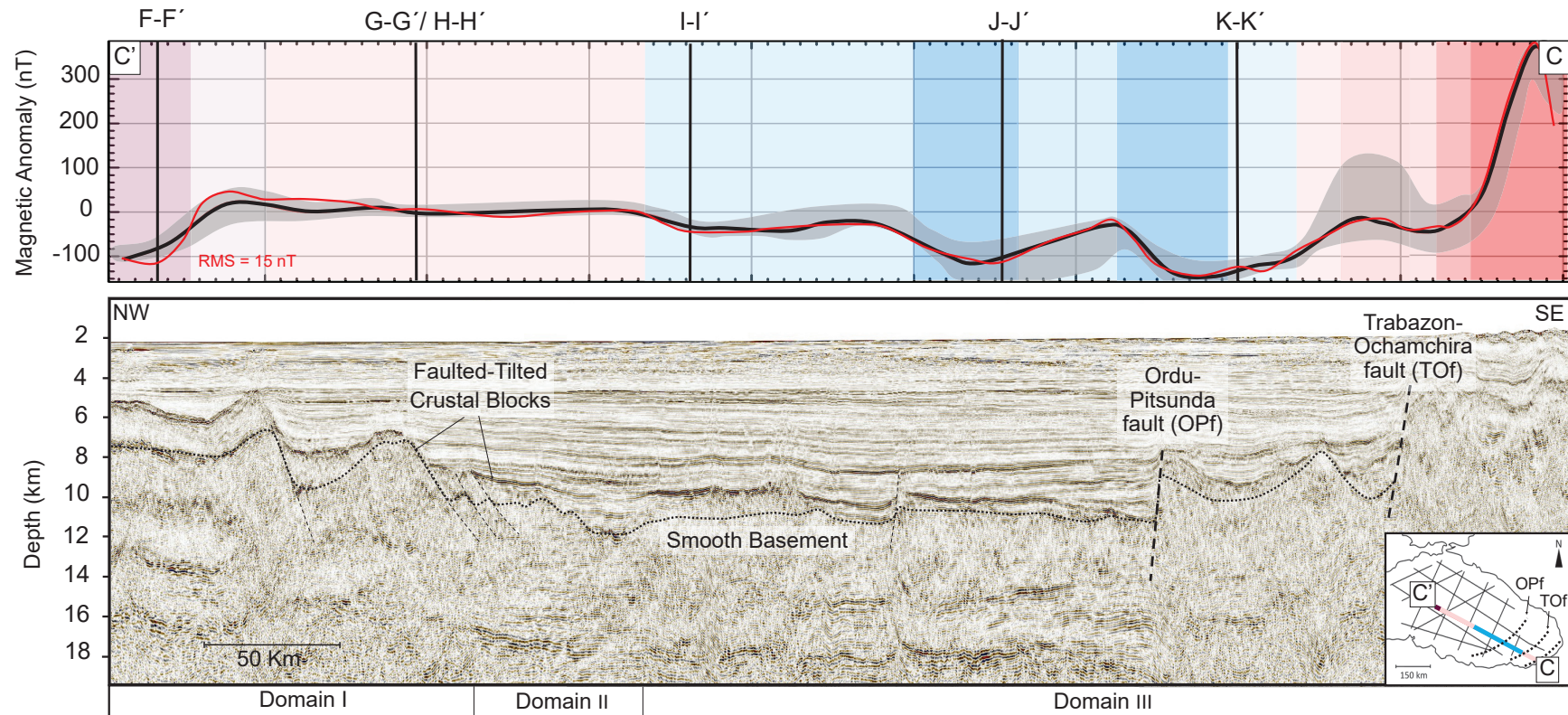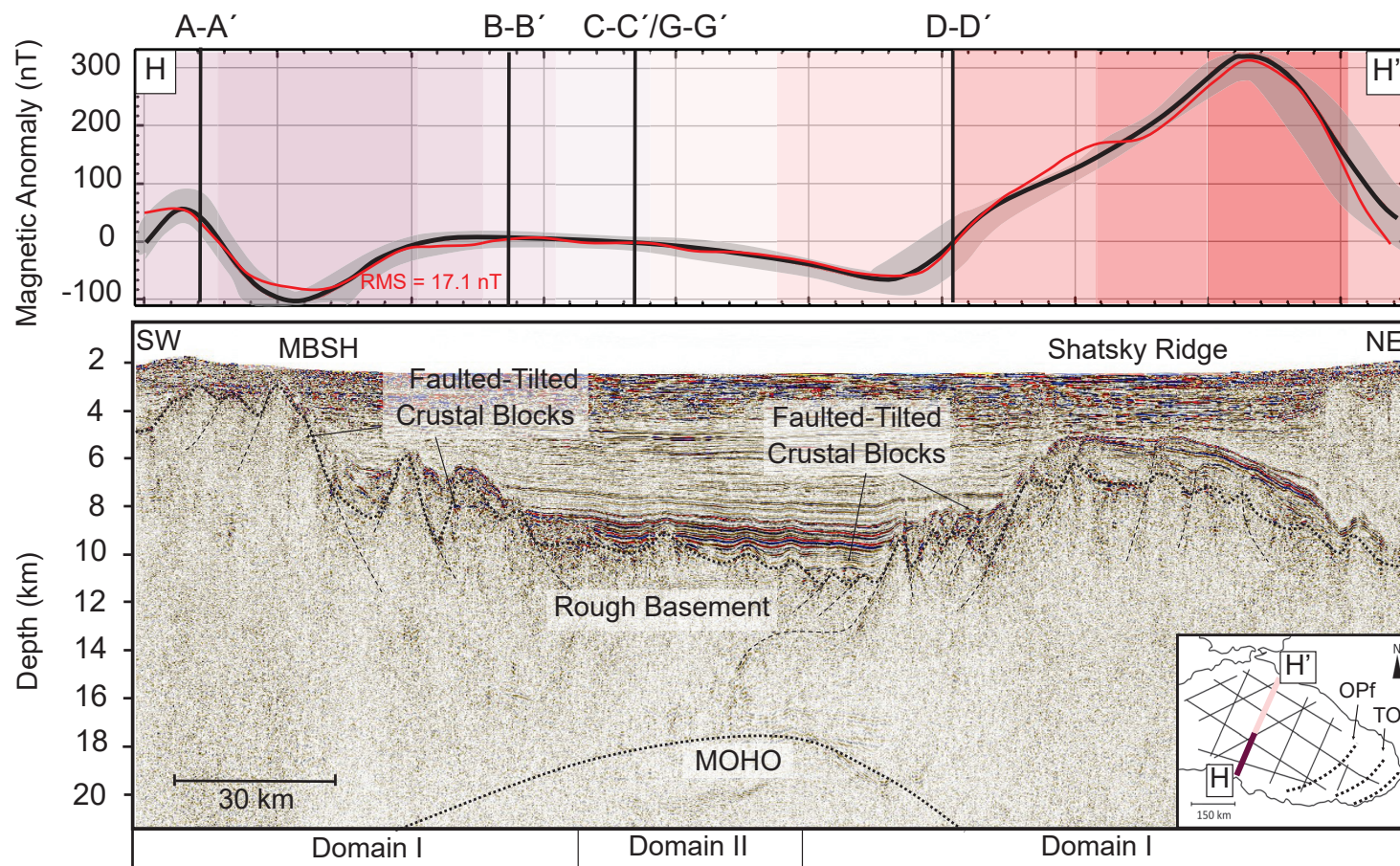
Figure DR4. Magnetic anomaly modelling along seismic profile bp-91-109. Top panel (Fig. DR2 - C-C') shows the observed (black) and calculated (red) anomaly along this profile. Magnetic intensity is indicated with colored bands (color scale as shown in Fig. DR2). Bottom panel shows bp-91-109 seismic profile. Top basement and fault systems interpreted are in overlay. The location map at the bottom right corner shows the profile position, with colors associated to the interpreted continental (pink-purple) and oceanic (blue) domains. Trans-tensional fault locations are also shown in the location map (OPf and TOf). (VE = 7).

Figure DR5. Magnetic anomaly modelling along seismic profile bs-90. Top panel (Fig. DR2 - H-H') shows the observed (black) and calculated (red) anomaly along this profile. Magnetic intensity is indicated with colored bands (color scale as shown in Fig. DR2). Bottom panel shows the bs-90 seismic profile. Top basement and fault systems interpreted are in overlay. Moho depth comes from Graham et al. (2013) gravity modelling. No oceanic crust is inferred in the central basin (Domain II), where a rough basement is instead associated with stretched continental crust based on the presence of weakly-magnetized layers. The location map at the bottom right corner shows the profile position, with colors marking the interpreted continental (pink-purple) domain. Trans-tensional fault locations are also shown in the location map (OPf and TOf). (VE = 5)
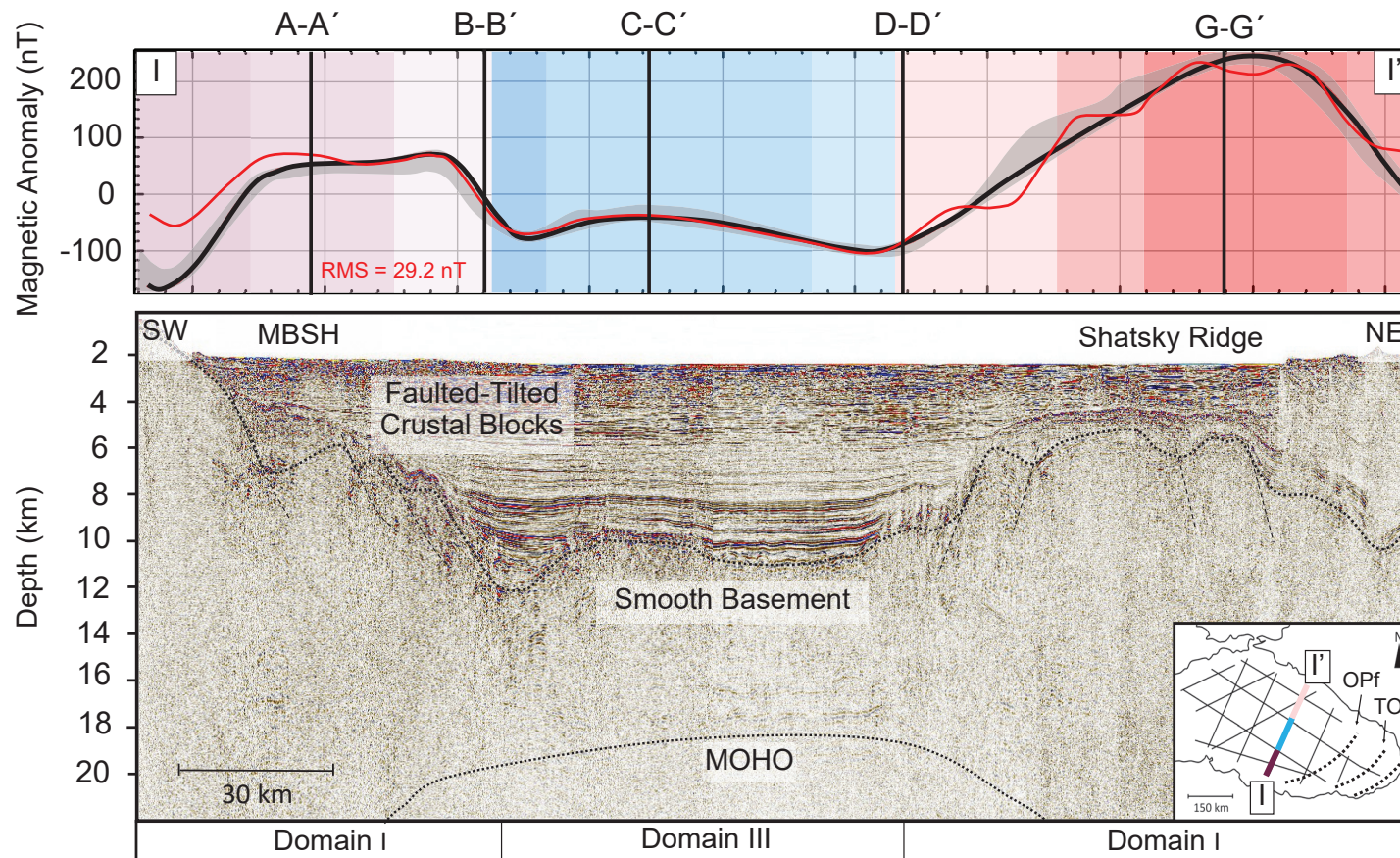
Figure DR6. Magnetic anomaly modelling along seismic profile bs-100. Top panel (Fig. DR2 - I-I') shows the observed (black) and calculated (red) anomaly along this profile. Magnetic intensity is indicated with colored bands (color scale as shown in Fig. DR2). Bottom panel shows the bs-100 seismic profile. Top basement and fault systems are interpreted in overlay. Moho depth comes from Graham et al. (2013) gravity modelling. Domain III is interpreted as an oceanic type of crust, due to its smooth morphology and the strong and negative magnetization character, with intensity between 1.6 and 2.4 A/m. The location map at the bottom right corner shows the profile position, with colors marking the interpreted continental (pink-purple) and oceanic (blue) domains. Trans-tensional fault locations are also shown in the location map (OPf and TOf). (VE = 5)
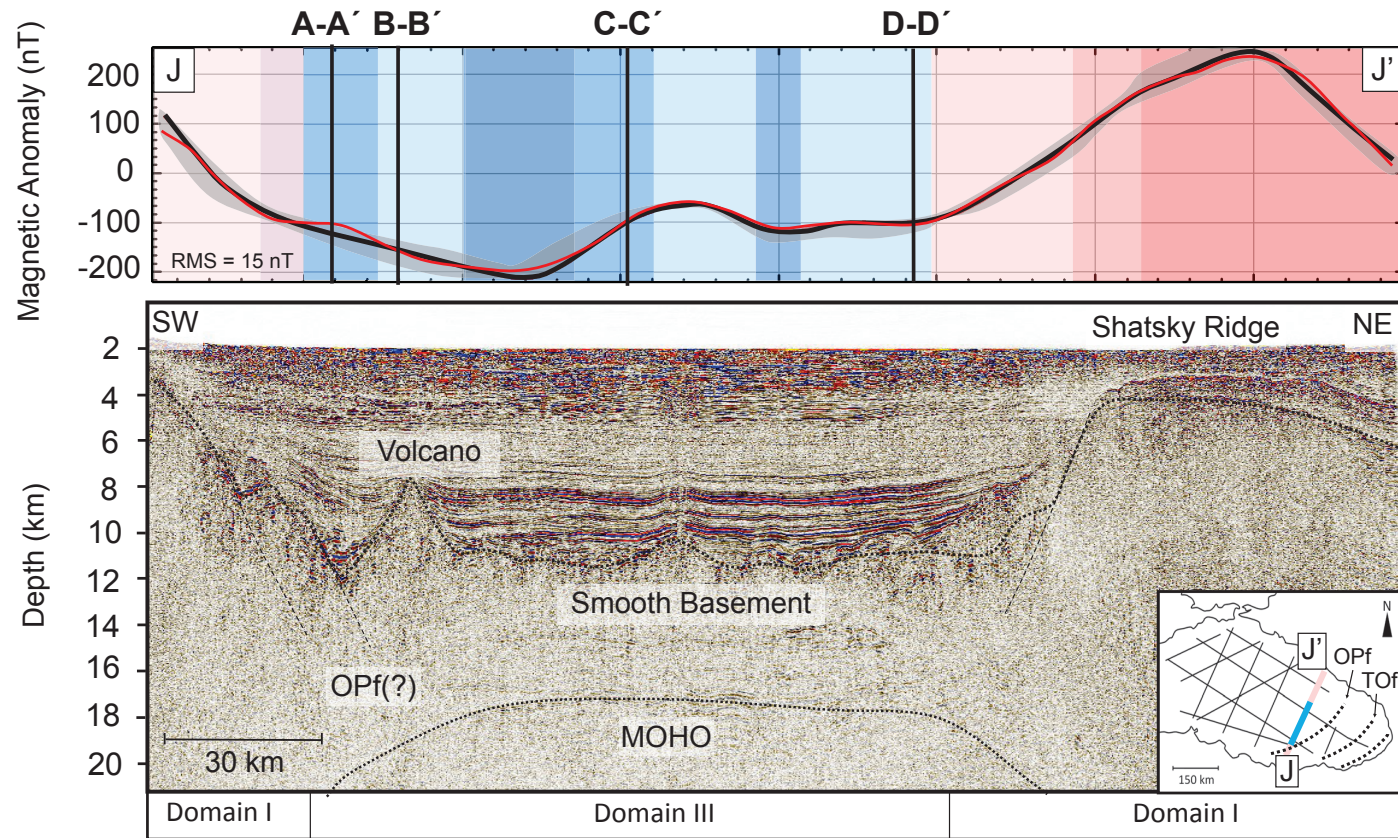
Figure DR7. Magnetic anomaly modelling along seismic profile bs-110. Top panel (Fig. DR2 - J-J') shows the observed (black) and calculated (red) anomaly along this profile. Magnetic intensity is indicated with colored bands (color scale as shown in Fig. DR2). Bottom panel shows the bs-110 seismic profile. Top basement and fault systems are interpreted in overlay. Moho depth comes from Graham et al. (2013) gravity modelling. Domain III is interpreted as oceanic crust, due to its smooth morphology and the strong and negative magnetization character, with intensity between 1.1 and 3.8 A/m. The location map at the bottom right corner shows the profile position, with colors marking the interpreted continental (pink-purple) and oceanic (blue) domains. Trans-tensional fault locations are also shown in the location map (OPf and TOf). (VE = 5)
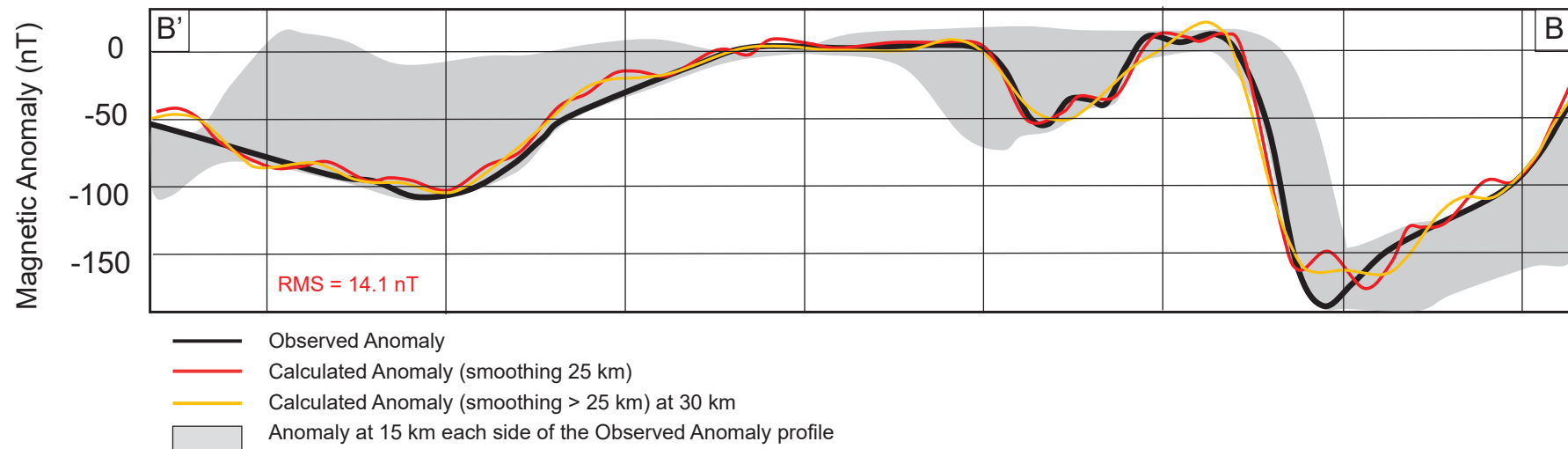
Figure DR8. Magnetic anomaly modelling along seismic profile bs-170 (Fig. DR2 - B-B'). A smoothing > 25 km over the calculated anomaly removes some of the features resolved by the observed anomaly.